Scaling behavior of low-temperature orthorhombic domains in the prototypical high-temperature superconductor $La_{1.875}Ba_{0.125}CuO_4$

T. A. Assefa,[1,*] Y. Cao,[1,2,†] J. Diao,[3] R. J. Harder,[4] W. Cha,[4] K. Kisslinger,[5] G. D. Gu,[1] J. M. Tranquada,[1] M. P. M. Dean,[1] and I. K. Robinson[1,3,‡]

[1]*Condensed Matter Physics and Materials Science Department, Brookhaven National Laboratory, Upton, New York 11973, USA*

[2]*Materials Science Division, Argonne National Laboratory, Lemont, Illinois 60439, USA*

[3]*London Centre for Nanotechnology, University College London, London WC1E 6BT, United Kingdom*

[4]*Advanced Photon Source, Argonne, Illinois 60439, USA*

[5]*Center for Functional Nanomaterials, Brookhaven National Laboratory, Upton, New York 11793, USA*

(Received 24 September 2019; revised manuscript received 22 January 2020; accepted 23 January 2020; published 11 February 2020)

Structural symmetry breaking and recovery in condensed-matter systems are closely related to exotic physical properties such as superconductivity (SC), magnetism, spin density waves, and charge density waves (CDWs). The interplay between different order parameters is intricate and often subject to intense debate, as in the case of CDW order and superconductivity. In $La_{1.875}Ba_{0.125}CuO_4$ (LBCO), the low-temperature structural domain walls are hypothesized as nanometer-scale pinning sites for the CDWs. Coherent x-ray diffraction techniques have been employed here to visualize the domain structures associated with these symmetry changes directly during phase transition. We have pushed Bragg coherent diffractive imaging (BCDI) into the cryogenic regime where most phase transitions in quantum materials reside. Utilizing BCDI, we image the structural evolution of LBCO microcrystal samples during the high-temperature tetragonal to low-temperature orthorhombic (LTO) phase transition. Our results show the formation of LTO domains close to the transition temperature and how the domain size decreases with temperature. The number of domains follows the secondary order parameter (or orthorhombic strain) measurement with a critical exponent that is consistent with the three-dimensional universality class.

DOI: 10.1103/PhysRevB.101.054104

I. INTRODUCTION

The phase diagrams of transition-metal oxides exhibit numerous electronic phases, often in close proximity to one another [1–7]. This subtle balance between the different electronic phases means that small changes in crystal structure can be sufficient to switch between different electronic phases. A notable example of this occurs in the cuprates [8], for which the prototypical example occurs in $La_{1.875}Ba_{0.125}CuO_4$ (LBCO). The emergence of charge density wave (CDW) order is closely tied to the lattice symmetry. LBCO has a high-temperature tetragonal (HTT) crystal structure at room temperature. Upon cooling, the low-temperature orthorhombic (LTO) structure emerges at a transition temperature of about 240 K, followed by a low-temperature tetragonal (LTT) phase with a transition temperature of 54 K. The HTT phase is characterized by untilted CuO_6 octahedra; in LTO they are tilted along the Cu-Cu bond direction, and in the LTT phase, they are tilted along the Cu-O bond direction [5,9–11]. The tilts in the LTT phase create lines of displaced O atoms that couple strongly to CDW order. This creates a remarkable enhancement of CDW order and a related strong suppression of bulk CDW order [5,9,12–16].

Soft x-ray coherent scattering experiments have shown that the CDW phase is quite static [17], and the CDW pinning landscape is inherited from a domain wall structure of the LTO phase [18]. Recently, a speckle correlation analysis on the $(012)_{LTO}$ superstructure peak showed that the diffraction patterns changed whenever the sample was heated above the HTT-LTO transition temperature, indicating that the LTO domains rearranged every time the LTO phase transition was crossed [19]. Characterizing the LTO domains in three dimensions is therefore central to understanding the physics behind the pinning phenomenon and the electronic ground state [20–22]. Here we use the Bragg coherent diffraction imaging (BCDI) technique to get real-space images of the domain texture in LBCO close to the LTO phase transition. This technique involves measuring a properly oversampled [23] diffraction pattern from a finite crystal fully illuminated with coherent x-ray. The measured diffraction pattern is then related to the Fourier transform of the electron density of the finite crystal. The phase information lost during the measurement can be retrieved with suitable phase retrieval algorithms [24–29].

In this paper, we present three-dimensional (3D) renderings of LTO domains within an LBCO single-crystal sample,

*tassefa@bnl.gov

†Present address: Materials Science Division, Argonne National Laboratory, Argonne, Illinois 60439, USA.

‡irobinson@bnl.gov

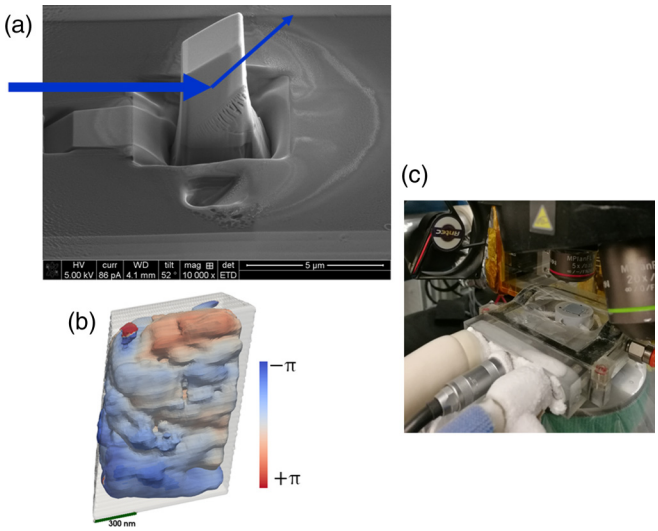

FIG. 1. (a) Scanning electron microscopy image of the $1.6 \times 1.6 \times 1.6$ μm^3 cube-shaped LBCO sample which was cut out of a preoriented single crystal using the FIB milling process. The arrows indicate the direction of the incoming and diffracted x-ray beam. (b) Isosurface rendering of the reconstructed image obtained after phase retrieval. (c) Picture of the Linkam stage during the BCDI experiment.

obtained using the BCDI technique [29–31]. Inverted images show the formation of domains when the sample temperature is below the HTT-LTO phase transition temperature. A slice through the rendered inverted images shows the internal structure of LTO domains and the domain walls formed along the $[110]_{HTT}$ as a stack. In addition, from reconstructed images, the estimated LTO domain size is between 200–400 nm at 228 K and is consistent with TEM results [22].

II. EXPERIMENTAL METHODS

A high-quality single crystal of LBCO was prepared using the floating-zone method [32]. To obtain the micron-size crystal needed for the BCDI study, the large LBCO crystal was oriented crystallographically using a Laue diffractometer. Then a $1.6 \times 1.6 \times 1.6$ μm^3 cube sample was cut out from the preoriented crystal via the *in situ* lift-out method utilizing the Omniprobe manipulation system and a Field Electron and Ion (FEI) Helios 600 dual-beam focused-ion beam (FIB; see Fig. 1) [33]. The size of the cube was chosen to be less than the extinction depth of 9-keV x rays in LBCO to minimize dynamical diffraction effects [34–36]. Then the sample was wielded with Pt onto a silicon wafer. This procedure was carried out at the Center for Functional Nanomaterials at Brookhaven National Laboratory (BNL). In addition to the Pt wielding, a solution of 2% tetraethyl orthosilicate in ethanol was drop casted on the LBCO cube and then annealed for about 5 hr at about 700 K in an oxygen atmosphere to avoid loss of oxygen during the annealing process. This method has been used for small metal nanocrystals and has proved to be an important step to keep the nanocrystals fixed during transportation and measurements [37]. Then the sample was mounted on a custom-modified Linkam stage for BCDI measurements where the flow of liquid nitrogen can be controlled precisely by the T96 controller to set a specific target temperature and program linear cooling ramps up to 373 K/min. The complete cooling system has a controller, a pump, the Linkam stage, and a liquid-nitrogen holder Dewar. The system allows cooling down to about 173 K, and low cooling rates give less icing and reduce noise and vibration.

Bragg coherent diffraction data were collected at the 34-ID-C beamline of the Advanced Photon Source. The beamline normally operates with a focused x-ray beam size of 600×600 nm^2 (V × H), which is smaller than the $1.6 \times 1.6 \times 1.6$ μm^3 LBCO cube sample. For valid imaging in Bragg coherent diffraction experiments, a monochromatic and coherent x-ray beam must surround the sample, so we used an unfocused beam size of 30×40 μm^2 (V × H) shaped with slits 200 mm in front of the sample. Since the sample was prealigned, the precise crystal alignment was quickly determined. Then coherent x-ray diffraction (CXD) patterns from the $(103)_{HTT}$ and $(114)_{HTT}$ Bragg peaks were acquired using a Timepix detector mounted at 2 m away from the sample. The full sensor of the detector has 512×512 pixels with a pixel size of 55 μm. Diffraction data were collected at each step while rocking the sample in increments of 0.0025° around the Bragg peak. Before feeding the CXD data to an iterative phasing algorithm developed in MATLAB [27,29,31,38], both white-field correction and hot pixel removal were applied for each diffraction pattern. For the phasing, a combination of error-reduction (ER) and hybrid-input-output algorithms [25,39] has been used alternately, with the iteration starting and ending with ER. The well-defined shapes and edges of the sample help to render the diffraction patterns invertible, which also allows us to use fixed box-shaped support to assist the phasing algorithms. This is an essential experimental advancement because the soft edges of even the best-focused x-ray beams are currently thought to be insufficiently sharp to use as support constraints [24,40]. Moreover, when the particle size is larger than both the longitudinal and transverse coherence lengths, the reconstructed images tend to have artifacts such as nonuniform amplitude distribution, with fewer facets and missing parts [41]. In our case, this was mitigated by turning on the partial coherence correction (PCC) in the iterative phasing algorithm at iteration 10 and then turned off at about one third of the way through the total iteration number [28,42].

III. BRAGG COHERENT DIFFRACTION IMAGING RESULTS

Our CXD results from the $(103)_{HTT}$ and $(114)_{HTT}$ structural Bragg peaks show similar behavior. As shown in Fig. 2, both diffraction peaks are split on the detector below 240 K, which is an indication of LTO twin-domain formation as reported from previous x-ray [10] and electron diffraction measurements [20,21,28,43–45]. Plots of the coherent diffraction patterns collected near the $(103)_{HTT}$ and $(114)_{HTT}$ Bragg reflections from the same sample are shown in Figs. 2(a)–2(d) and 2(e)–2(h), respectively. Initially, both $(103)_{HTT}$ and $(114)_{HTT}$ diffraction peaks broaden as the sample temperature decreases. Then both the $(103)_{HTT}$ and $(114)_{HTT}$ diffraction peaks become split when the temperature falls below 240(5) K. At all temperatures, both diffraction peaks are strongly

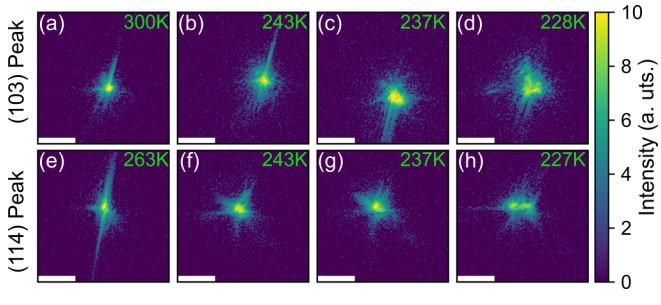

FIG. 2. (a)–(f) Logarithmic-scale plots of coherent diffraction peaks are measured (a)–(d) using the $(103)_{\mathrm{HTT}}$ Bragg peak and (e)–(f) using the $(114)_{\mathrm{HTT}}$ Bragg peak of the same LBCO sample measured at different temperatures. The scale bar shown is 40 pixels, corresponding to 1×10^{-1} nm^{-1}. Both δq_x and δq_y are mutually perpendicular reciprocal space vectors coplanar to the CCD surface and calculated as $(2\pi/\lambda)(p/D)$, where $\lambda = 1.3776$ Å is the wavelength, $p = 55$ μm is detector pixel size, and $D = 2$ m is the sample-to-detector distance.

speckled on the detector because of the high coherence of the beam and stability of the 34-ID-C setup. The diffraction peak splitting temperature is consistent with the HTT-LTO transition temperature, reported from previous x-ray and neutron measurements [5,9,10].

Moreover, 3D diffraction data were collected from both Bragg reflections at several temperatures spanning the HTT to LTO phase transition. From the white-field- and flat-field-corrected images two regions of interest, ROI1 and ROI2, were integrated over the Bragg peak and far away for the background subtraction, respectively, and difference plotted as rocking curves, shown in Figs. 3(a) and 3(b). Similar to what we observed in the two-dimensional (2D) diffraction data, the rocking curves also show peak splitting. The $(103)_{\mathrm{HTT}}$ peak splits into multiple peaks on the detector as the sample temperature decreases continuously, whereas the $(114)_{\mathrm{HTT}}$ peak has a tiny peak on the left side the rocking

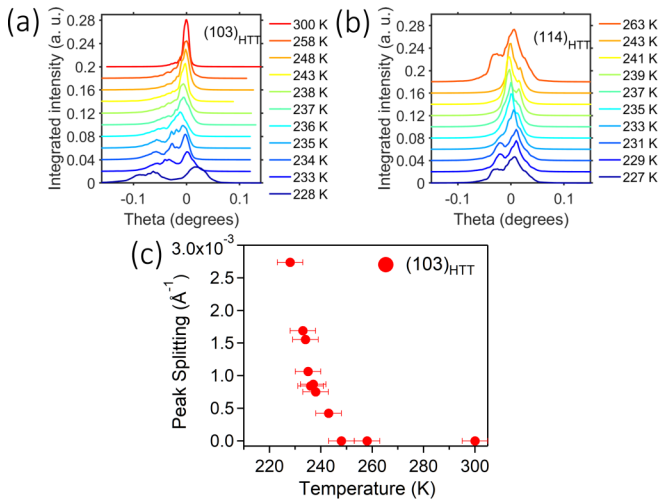

FIG. 3. (a) and (b) Rocking curves of $(103)_{\mathrm{HTT}}$ and $(114)_{\mathrm{HTT}}$ background-subtracted integrated Bragg peaks as a function of temperature measured during the HTT to LTO phase transition. (c) Total three-dimensional $(103)_{\mathrm{HTT}}$ diffraction peak splitting.

curve in the HTT phase, indicating inhomogeneity possibly introduced during ion milling of the sample. As a result, both the peak splitting analysis and reconstruction will focus on the $(103)_{\mathrm{HTT}}$ Bragg peak data. To calculate the total peak splitting displacement Δq for the $(103)_{\mathrm{HTT}}$ peak, first, we recorded the difference in pixel position Δp_x and Δp_y on the detector and the frame number Δp_z for all temperatures. We convert the difference in pixels and frame number to Å^{-1} as $\Delta q_x = (2\pi/\lambda)(p/D)\Delta p_x$, $\Delta q_y = (2\pi/\lambda)(p/D)\Delta p_y$, and $\Delta q_z = Q\Delta\theta\Delta p_z$, where λ is the x-ray wavelength, Q is the momentum transfer, p is the pixel size, D is the detector distance, and $\Delta\theta$ is the step size of the rocking scan. Finally, the three-dimensional peak splitting shown in Fig. 3(c) is calculated as $\Delta q = \sqrt{(\Delta q_x^2 + \Delta q_y^2 + \Delta q_z^2)}$. Figure 3(c) shows that the peak splitting disappears at the expected HTT-LTO transition temperature, indicating the formation of $(113)_{\mathrm{LTO}}$ rotated twins domains. Moreover, the splitting onset temperature determined from the rocking curves shown in Figs. 3(a) and 3(b) differs slightly between the $(103)_{\mathrm{HTT}}$ peak at 234 K and $(114)_{\mathrm{HTT}}$ at 235 K, which we attribute to a finite uncertainty in the measurement such as temperature offset between the sample and temperature recorded by Linkam cooling stage sensor.

We interpret the peak splitting as being due to a/b twinning in the orthorhombic phase of LBCO and can use BCDI to obtain images of the pattern of domains in three dimensions. In order to visualize the evolution of LTO domain formation close to the transition temperature, we inverted the 3D coherent diffraction patterns using iterative phasing. The reconstruction results in Fig. 4 show a clear difference between the LTO and HTT phases reconstructed from the 228 and 258 K temperature data. To understand better the internal structure of the phases, we take a slice cut through the reconstructed image in the [100] plane. At 258 K the slice shows a "single" domain, whereas at 228 K, it shows the presence of several domains with sizes in the range of 150–350 nm. There is a phase ramp between the domains which has a size of 20–50 nm. These domain and domain-wall sizes are close to those reported in electron microscopy studies of LBCO [20,43]. In addition, our results are also close to domain sizes reported in $La_{1.8}Sr_{0.12}CuO_4$ [22,43] and $La_{1.725}Sr_{0.275}NiO_4$ [46] from electron microscopy studies. To make a comparison with TEM dark-field results we take a slice along the [001] plane of 228 K data, and the result is shown in Fig. S2 in the Supplemental Material [47]. Similar layerlike domains are observed, which are elongated in one direction. The domain and domain-wall sizes obtained from our reconstruction results are on the same order of magnitude as the TEM results. Furthermore, we present the 235 K data in a similar fashion (see Fig. S1 in the Supplemental Material [47]); the data show the domain size is larger than the 228 K data and domains are stacked in a similar way. To look at the amplitude and phase variation inside the reconstructed images of HTT and LTO phases, line profiles through [001] slices are shown in Figs. S3 and S4.

Because the crystal is isolated at the center of the diffractometer, samples prepared through FIB give us an opportunity to measure multiple peaks from the same crystal without any contaminating signals from neighboring crystals. In the future

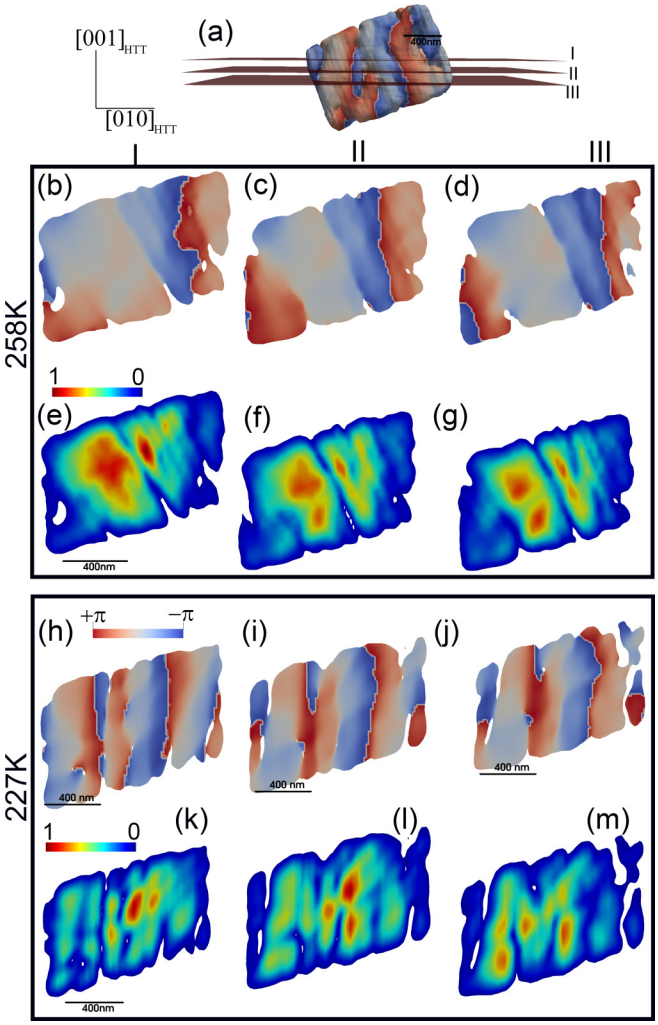

FIG. 4. (a) Isosurface representation of the reconstructed LBCO single crystal. Red planes I, II, and III show the spatial location where the slices are taken. (b)–(d)The phase (projection of the lattice displacement) and (e)–(g) amplitude (electron density) for the reconstructed particle for the high-temperature-tetragonal phase. (h)–(j) The phase (projection of the lattice displacement) and (k)–(m) amplitude (electron density) for the reconstructed particle for the low-temperature-orthorhombic phase.

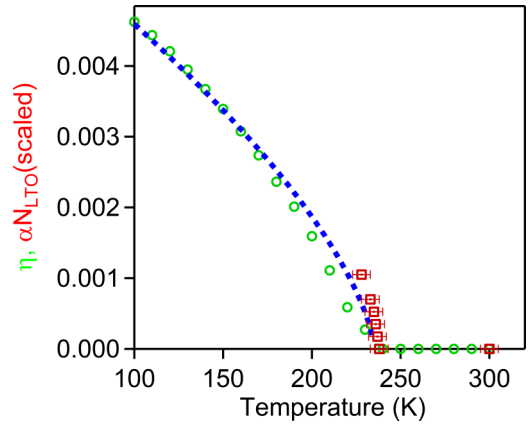

FIG. 5. Temperature evolution of lattice strain η calculated as $\frac{2(a-b)}{(a+b)}$; the lattice parameters are derived from Rietveld refinements [9] (green circles). The temperature evolution of the number of domains N_{LTO} is extracted from reconstructed 3D images and counted by visualizing in PARAVIEW. Data shown by red squares are scaled number of domains as αN_{LTO}, with $\alpha = 1.75 \times 10^{-4}$. We also plotted the $\gamma(T_c - T)^{2\beta}$ function with $T_c = 238$ K and $\beta = 0.33$ as a guide to the eye (blue dashed line).

this has a potential application for quantum materials where one can image a single FIB crystal using both structural and electronic order peaks and overlay reconstructed real-space images. However, the ion-milling process can also introduce undesired damage, an amorphization layer, and strain on the surface of the sample, or it can affect the chemical composition. Typically, the damage of the FIB sample is 20 to 30 nm for 30-keV Ga ions, and 5-keV ions would have a three times smaller effect [48]. Also, how far the Ga ions penetrate the sample depends on both the energy of ions and the angle of polishing (normal incidence versus glancing incidence) [49]. For gold nanocrystals, Ga ions can go up to 50 nm at 30 keV and normal incidence and decrease by a factor of 5 at 5 keV and glancing incidence [49]. Although we used the 5-keV ion beam for final polishing of the present sample to minimize the damage, amorphization layer, and strain, some of the strains and nonsharp edges could be partly due to the beam-milling process.

BCDI reconstructed images allow us to count domains in three dimensions [50]. Figure 5 shows that the number of domains increases dramatically when the sample temperature is below the HTT-LTO transition temperature. An early Ginzburg-Landau study of the HTT-LTO transition derived the critical behavior of the orthorhombicity near the LTO transition temperature with the critical exponent $\beta = 0.33$ [51].

Domain indexing by Fourier filtering

The complex pattern of domains seen in the low-temperature orthorhombic phase is believed to be due to twinning between regions of opposite orientation of their a and b axes [52]. The diffraction peak splitting at low temperatures arises for the same reason. BCDI opens a unique opportunity to assign which domain in the image arises from which peak in the diffraction pattern. This is undertaken in Figs. 6 and 7 to test the idea.

The final 3D image of the domains at the lowest temperature, measured at the $(103)_{\mathrm{HTT}}$ diffraction peak, was Fourier transformed back to reciprocal space to regenerate the split diffraction peak while retaining all the phase information. A region of $21 \times 21 \times 25$ voxels was set to zero around the first diffraction peak, and it was inverse Fourier transformed to give an image with all the domains contributing to that peak suppressed. This was repeated for the second Bragg peak by setting $13 \times 13 \times 13$ voxels to zero. The results are shown in Fig. 6 in the raw coordinate system of the discrete Fourier transform of the data voxels, (x, y) detector pixels and z steps on the rocking curve. The (x, y, z) directions are roughly aligned with the Cartesian (x, y, z) coordinate system used in Fig. 4. The z slices shown in Fig. 6 show cross sections of the sample roughly perpendicular to the x-ray beam direction. The

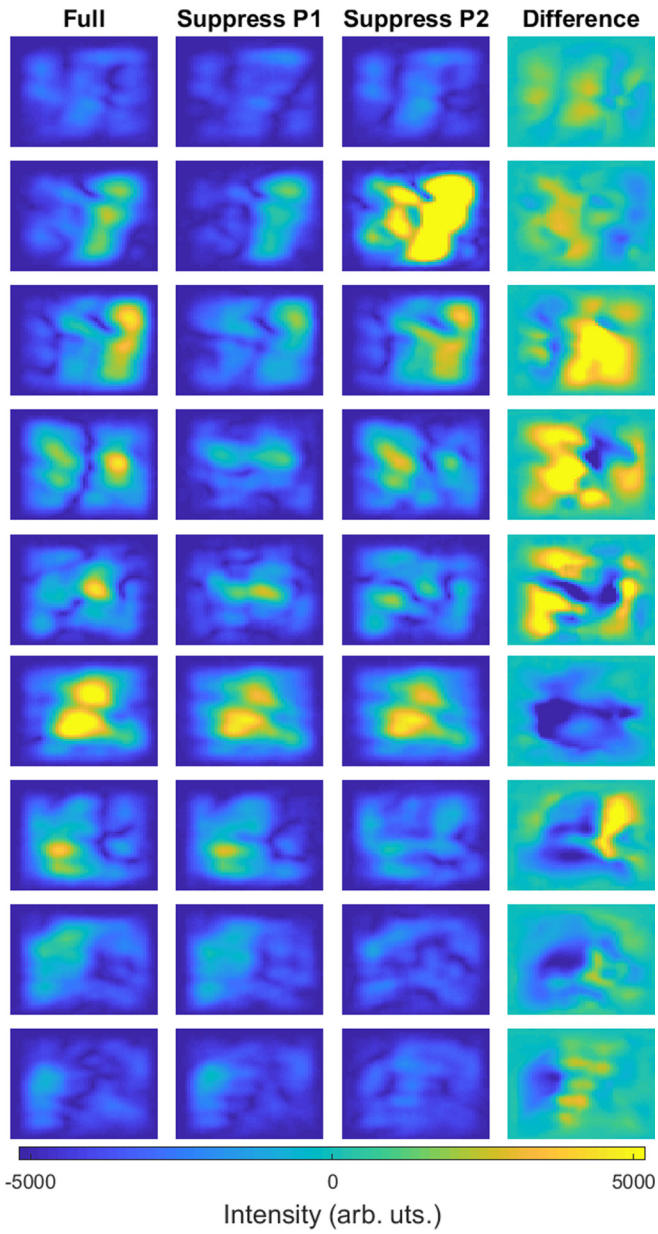

FIG. 6. Fourier filtering on the reconstructed image of the LBCO single crystal measured at 228 K of the different slices along the third dimension. Suppress P1 is obtained by Fourier filtering of $21 \times 21 \times 25$ voxels around the smaller peak by setting it to zero for reconstruction. Suppress P2 is obtained by Fourier filtering of $13 \times 13 \times 13$ voxels around the larger peak by setting to zero for reconstruction.

image amplitude is presented on the same color scale of 0 to 1.6×10^4 in the first three columns for a selection of z slices, whereas the difference between suppress P1 and suppress P2 is shown on a scale of -5.2×10^4 to 5.2×10^4. It can be seen that different parts of the initial domain image (left) become reduced in amplitude in the two derived images of suppress P1 and suppress P2.

To visualize the domain identities more clearly, a color image was generated in the same physical "laboratory" Cartesian coordinate frame already used to present the images in

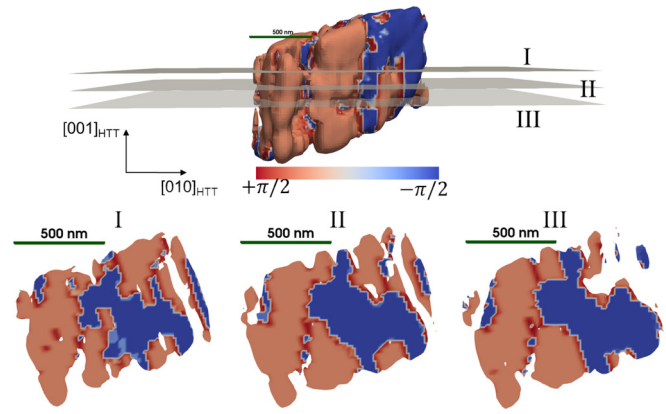

FIG. 7. Isosurface representation of the reconstructed LBCO single-crystal domains measured at 228 K. Gray planes, denoted I, II, and III, are the spatial locations where slices are extracted and are displayed below to show which peak the domains contribute to the reconstructed domains. The red or blue color indicates whether the image amplitude is higher with the first or second peak suppressed.

Fig. 4. Here, z runs along the beam, x is horizontal, transverse to the beam, and y is vertical. In Fig. 7 an isosurface of the crystal and three slices through the 3D image are shown, corresponding to the views of Figs. 4(k)–4(m). The domains are colored red or blue according to whether their amplitude is higher with the first or second peak suppressed.

There is a clear pattern in these images where domains are color-coded according to the diffraction peak to which they contribute most. It appears that one end of the crystal mostly contributes to the "blue" peak and the other end contributes mainly to the "red" peak. In between, there is some alternation of domain identities, as expected from the microtwinning concept [52]. This result strongly supports the picture of twinning underlying formation of domains in the LBCO tetragonal to orthorhombic phase transition.

IV. CONCLUSION AND OUTLOOK

The coherent x-ray diffraction technique allows us to track the evolution of structural domains by monitoring a shared Bragg diffraction peak on a 2D detector. The transition temperature deduced agrees with previously published x-ray studies [5,9]. Moreover, the speckle pattern in reciprocal space is a unique fingerprint of how domains are staggered in the sample (real space), and both $(103)_{HTT}$ and $(114)_{HTT}$ diffraction patterns split into multiple peaks, indicating the formation of twin domains. This behavior of the splitting crystal peaks agrees with the recent observation of rearrangement of the speckles at the $(012)_{LTO}$ superstructure peak that is unique to the low-temperature phase [19]. Speckle correlation analysis clearly shows that a different LTO domain configuration is obtained every time the phase transition is crossed.

In the BCDI technique, the phase information lost during the measurement is retrieved using the computational technique with properly oversampled diffraction patterns; one can iteratively reconstruct the phase. For weak phasing

objects such as metal nanoparticles [29,31,53], battery materials [54,55], and oxides [56], the retrieved real-space images give internal strain information in addition to electron density, which is not accessible with any other technique [57]. However, imaging structural texture of strongly correlated materials presents a challenge to the technique, and obtaining a unique solution is very challenging. To circumvent this issue, we implemented a fixed-box support constraint in the iterative phasing algorithm which allowed us to invert the reciprocal diffraction patterns to real-space images and gave a reproducible result. The reconstructed real-space images of domains we observed are LTO twin domains, which are very common for this type of sample. Neighboring domains showed a phase shift, and the phase difference between the two nearby domains gave the relative displacement of twin domain walls. The observation of LTO domains agrees with previous "microstructures" (domains) of $La_{2-x}Sr_xCuO_4$ [21,22] and LTO $La_{2-x}Ba_xCuO_4$ [20] obtained with dark-field transmission electron microscopy. As shown in Fig. 5, the number of domains follows a path similar to the degree of orthorhombicity (orthorhombic strain) derived from powder diffraction data [9], which is related to the order parameter [58].

ACKNOWLEDGMENTS

We want to thank M. Hu, D. Mazzone, and E. Bozin for their insight on the experimental results. We also would like to thank E. Maxey for his support during the beam time and for his help in setting up the Linkam cooling stage for experiments at 34-ID-C. T.A.A. would like to thank F. Hofmann for his comments on the experimental results and insights on focused ion-beam milling processes. X-ray experiments are supported by the US Department of Energy, Office of Science, Basic Energy Sciences, Materials Science and Engineering Division, under Contracts No. DE-SC0012704(BNL) and No. DE-AC02-06CH11357(ANL). The focused-ion beam sample preparation used the resources of the Center for Functional Nanomaterials, which is a US DOE Office of Science Facility, at BNL under Contract No. DE-SC0012704. The experiments were carried out at Advanced Photon Source (APS) beamline 34-ID-C, and the APS was supported by the US Department of Energy, Office of Science, Office of Basic Energy Sciences, under Contract No. DE-AC02-06CH11357. The beamline 34-ID-C was built with US National Science Foundation Grant No. NSF-DMR 9724294 Development of a Coherent X-Ray Diffraction Instrument 09/15/1997.

[1] S. A. Kivelson, I. P. Bindloss, E. Fradkin, V. Oganesyan, J. M. Tranquada, A. Kapitulnik, and C. Howald, Rev. Mod. Phys. **75**, 1201 (2003).

[2] E. Dagotto, T. Hotta, and A. Moreo, Phys. Rep. **344**, 1 (2001).

[3] B. Keimer, S. A. Kivelson, M. R. Norman, S. Uchida, and J. Zaanen, Nature (London) **518**, 179 (2015).

[4] J. M. Tranquada, G. D. Gu, M. Hücker, Q. Jie, H.-J. Kang, R. Klingeler, Q. Li, N. Tristan, J. S. Wen, G. Y. Xu *et al.*, Phys. Rev. B **78**, 174529 (2008).

[5] M. Hücker, M. v. Zimmermann, G. D. Gu, Z. J. Xu, J. S. Wen, G. Xu, H. J. Kang, A. Zheludev, and J. M. Tranquada, Phys. Rev. B **83**, 104506 (2011).

[6] R. Comin and A. Damascelli, Annu. Rev. Condens. Matter Phys. **7**, 369 (2016).

[7] Q. Li, M. Hücker, G. D. Gu, A. M. Tsvelik, and J. M. Tranquada, Phys. Rev. Lett. **99**, 067001 (2007).

[8] J. M. Tranquada, B. J. Sternlieb, J. D. Axe, Y. Nakamura, and S. Uchida, Nature (London) **375**, 561 (1995).

[9] E. S. Bozin, R. Zhong, K. R. Knox, G. Gu, J. P. Hill, J. M. Tranquada, and S. J. L. Billinge, Phys. Rev. B **91**, 054521 (2015).

[10] J. D. Axe, A. H. Moudden, D. Hohlwein, D. E. Cox, K. M. Mohanty, A. R. Moodenbaugh, and Y. Xu, Phys. Rev. Lett. **62**, 2751 (1989).

[11] A. J. Achkar, M. Zwiebler, C. McMahon, F. He, R. Sutarto, I. Djianto, Z. Hao, M. J. P. Gingras, M. Hücker, G. D. Gu *et al.*, Science **351**, 576 (2016).

[12] G. Fabbris, M. Hücker, G. D. Gu, J. M. Tranquada, and D. Haskel, Phys. Rev. B **88**, 060507(R) (2013).

[13] M. Fujita, H. Goka, K. Yamada, J. M. Tranquada, and L. P. Regnault, Phys. Rev. B **70**, 104517 (2004).

[14] S. B. Wilkins, M. P. M. Dean, J. Fink, M. Hücker, J. Geck, V. Soltwisch, E. Schierle, E. Weschke, G. Gu, S. Uchida *et al.*, Phys. Rev. B **84**, 195101 (2011).

[15] H. Miao, J. Lorenzana, G. Seibold, Y. Y. Peng, A. Amorese, F. Yakhou-Harris, K. Kummer, N. B. Brookes, R. M. Konik, V. Thampy *et al.*, Proc. Natl. Acad. Sci. USA **114**, 12430 (2017).

[16] H. Miao, R. Fumagalli, M. Rossi, J. Lorenzana, G. Seibold, F. Yakhou-Harris, K. Kummer, N. B. Brookes, G. D. Gu, L. Braicovich, G. Ghiringhelli, and M. P. M. Dean, Phys. Rev. X **9**, 031042 (2019).

[17] X. M. Chen, V. Thampy, C. Mazzoli, A. M. Barbour, H. Miao, G. D. Gu, Y. Cao, J. M. Tranquada, M. P. M. Dean, and S. B. Wilkins, Phys. Rev. Lett. **117**, 167001 (2016).

[18] X. M. Chen, C. Mazzoli, Y. Cao, V. Thampy, A. M. Barbour, W. Hu, M. Lu, T. A. Assefa, H. Miao, G. Fabbris *et al.*, Nat. Commun. **10**, 1435 (2019).

[19] I. Robinson, T. A. Assefa, Y. Cao, G. Gu, R. Harder, E. Maxey, and M. P. M. Dean, J. Supercond. Novel Magn. **33**, 99 (2020).

[20] Y. Zhu, A. R. Moodenbaugh, Z. X. Cai, J. Tafto, M. Suenaga, and D. O. Welch, Phys. Rev. Lett. **73**, 3026 (1994).

[21] Y. Horibe, Y. Inoue, and Y. Koyama, Phys. C (Amsterdam, Neth.) **282–287**, 1071 (1997).

[22] Y. Horibe, Y. Inoue, and Y. Koyama, Phys. Rev. B **61**, 11922 (2000).

[23] C. E. Shannon, Proc. Inst. Radio Eng. **37**, 10 (1949).

[24] J. R. Fienup, Opt. Lett. **3**, 27 (1978).

[25] R. W. Gerchberg and W. O. Saxton, OPTIK **35**, 237 (1972).

[26] J. Miao, P. Charalambous, J. Kirz, and D. Sayre, Nature (London) **400**, 342 (1999).

[27] I. K. Robinson, I. A. Vartanyants, G. J. Williams, M. A. Pfeifer, and J. A. Pitney, Phys. Rev. Lett. **87**, 195505 (2001).

[28] I. A. Vartanyants and I. K. Robinson, J. Phys.: Condens. Matter **13**, 10593 (2001).

[29] I. Robinson and R. Harder, Nat. Mater. **8**, 291 (2009).
[30] I. Robinson, J. Clark, and R. Harder, J. Opt. **18**, 054007 (2016).
[31] M. A. Pfeifer, G. J. Williams, I. A. Vartanyants, R. Harder, and I. K. Robinson, Nature (London) **442**, 63 (2006).
[32] G. Gu, K. Takamuku, N. Koshizuka, and S. Tanaka, J. Cryst. Growth **130**, 325 (1993).
[33] F. Hofmann, E. Tarleton, R. J. Harder, N. W. Phillips, P.-W. Ma, J. N. Clark, I. K. Robinson, B. Abbey, W. Liu, and C. E. Beck, Sci. Rep. **7**, 45993 (2017).
[34] W. Hu, X. Huang, and H. Yan, J. Appl. Crystallogr. **51**, 167 (2018).
[35] M. Civita, A. Diaz, R. J. Bean, A. G. Shabalin, O. Y. Gorobtsov, I. A. Vartanyants, and I. K. Robinson, Phys. Rev. B **97**, 104101 (2018).
[36] A. G. Shabalin, O. M. Yefanov, V. L. Nosik, V. A. Bushuev, and I. A. Vartanyants, Phys. Rev. B **96**, 064111 (2017).
[37] M. Monteforte, A. K. Estandarte, B. Chen, R. Harder, M. H. Huang, and I. K. Robinson, J. Synchrotron Radiat. **23**, 953 (2016).
[38] I. K. Robinson, Z. Kristallogr. Suppl. **27**, 27 (2008).
[39] J. R. Fienup, Appl. Opt. **21**, 2758 (1982).
[40] J. R. Fienup, J. Opt. Soc. Am. A **4**, 118 (1987).
[41] S. J. Leake, M. C. Newton, R. Harder, and I. K. Robinson, Opt. Express **17**, 15853 (2009).
[42] J. Clark, X. Huang, R. Harder, and I. Robinson, Nat. Commun. **3**, 993 (2012).
[43] C. Chen, S.-W. Cheong, D. Werder, A. Cooper, and L. Rupp, Phys. C (Amsterdam, Neth.) **175**, 301 (1991).
[44] C. Chen, S.-W. Cheong, D. Werder, and H. Takagi, Phys. C (Amsterdam, Neth.) **206**, 183 (1993).
[45] C. H. Chen, S. Mori, and S.-W. Cheong, Phys. Rev. Lett. **83**, 4792 (1999).
[46] J. Li, Y. Zhu, J. M. Tranquada, K. Yamada, and D. J. Buttrey, Phys. Rev. B **67**, 012404 (2003).
[47] See Supplemental Material at http://link.aps.org/supplemental/10.1103/PhysRevB.101.054104 for two-dimensional slices and line profiles of the reconstructed images of LBCO in the HTT and LTO phases.
[48] N. I. Kato, J. Electron Microsc. **53**, 451 (2004).
[49] F. Hofmann, R. J. Harder, W. Liu, Y. Liu, I. K. Robinson, and Y. Zayachuk, Acta Mater. **154**, 113 (2018).
[50] J. Ahrens, B. Geveci, and C. Law, *ParaView: An End-User Tool for Large Data Visualization, Visualization Handbook* (Elsevier, Oxford, UK, 2005), pp. 717–731.
[51] R. J. Birgeneau, C. Y. Chen, D. R. Gabbe, H. P. Jenssen, M. A. Kastner, C. J. Peters, P. J. Picone, T. Thio, T. R. Thurston, H. L. Tuller *et al.*, Phys. Rev. Lett. **59**, 1329 (1987).
[52] A. M. Bratkovsky, H. Volker, and E. K. H. Salje, Philos. Trans. R. Soc. London, Ser. A **354**, 2875 (1996).
[53] M. C. Newton, R. Harder, X. Huang, G. Xiong, and I. K. Robinson, Phys. Rev. B **82**, 165436 (2010).
[54] A. Singer, M. Zhang, S. Hy, D. Cela, C. Fang, T. A. Wynn, B. Qiu, Y. Xia, Z. Liu, A. Ulvestad *et al.*, Nat. Energy **3**, 641 (2018).
[55] A. Ulvestad, A. Singer, J. N. Clark, H. M. Cho, J. W. Kim, R. Harder, J. Maser, Y. S. Meng, and O. G. Shpyrko, Science **348**, 1344 (2015).
[56] I. K. Robinson, J. L. Libbert, I. A. Vartanyants, J. A. Pitney, D. M. Smilgies, D. L. Abernathy, and G. Grübel, Phys. Rev. B **60**, 9965 (1999).
[57] J. Miao, T. Ishikawa, I. K. Robinson, and M. M. Murnane, Science **348**, 530 (2015).
[58] P. M. Chaikin and T. C. Lubensky, *Principles of Condensed Matter Physics* (Cambridge University Press, Cambridge, 1995).